SCIENCE CHINA
Technological Sciences

•Article•

April 2024 Vol.67 No.4: 1185–1195
https://doi.org/10.1007/s11431-023-2581-9

A compact bimorph rotary piezoelectric actuator with customized small power supply

DENG Jie†, LIU DaQing†, WANG WeiYi† & LIU YingXiang*

School of Mechatronics and Engineering, Harbin Institute of Technology, Harbin 150001, China

Received September 18, 2023; accepted December 29, 2023; published online March 22, 2024

Inertial piezoelectric actuators are widely applied in precision devices with simple structure and accurate movement. However, existing inertial piezoelectric actuators still face the challenges of rollback motion and bulky power supply. In this work, an alternate excitation strategy and a customized small power supply for a bimorph rotary piezoelectric actuator (BRPA) are proposed to solve the problems. The BRPA prototype is designed with a bipedal symmetrical structure, measuring 35 mm in height and 32 mm in diameter, which has a maximum rotation velocity of 0.247 rad/s and a resolution of 0.66 μrad. Thanks to the bipedal symmetrical structure, the friction directions between the driving feet and the rotor can be coordinated to suppress the rollback. The rollback ratio is almost zero when the phase difference of the exciting signal is set as 180°. The customized power supply is designed and manufactured, whose size is 58 mm×56 mm×46 mm. It can output signals for the single step mode and the continuous mode, and they are adopted to excite BRPA to achieve a small stroke with one single step and a large stroke with continuous step, respectively. Then, an experimental system for optical fiber alignment is developed based on the BRPA and the customized small power supply, the experiment has verified the practicability of this work in the precision fields, especially in the miniaturized precision systems.

inertial piezoelectric actuator, customized small power supply, single step mode, continuous mode, rollback suppression, miniaturized precision system

Citation: Deng J, Liu D Q, Wang W Y, et al. A compact bimorph rotary piezoelectric actuator with customized small power supply. Sci China Tech Sci, 2024, 67: 1185–1195, https://doi.org/10.1007/s11431-023-2581-9

1 Introduction

High precision driving technology is urgently needed in fields such as aerospace, micro-electronics, microfluidic, micro-optical systems, biomedical, etc. [1–5]. The rapid development of these fields requires accurate and stable motion at micrometer/nanometer level, large motion range, fast response speed, and sufficient load capacity [6]. To a certain degree, the traditional electromagnetic actuator with appropriate control strategy may meet the requirements of micromanipulation and precision position tasks [7]. However, the accuracy of positioning is significantly influenced by the clearance of the transmission system, which restricts its utilization in the above scenarios.

In recent decades, researchers have made significant advancements in the field of novel actuators, which have largely relieved the limitations of traditional actuators. Various types of actuators have been developed, including electrostatic actuators, electrothermal actuators, and piezoelectric actuators. Electrostatic actuators are renowned for the energy efficiency, fast response, and on-chip integration. However, strict sealing is necessary because of their susceptibility to environmental factors, such as dust and moisture. Besides, the pull-in phenomenon of electrostatic actuators leads to motion instability [8,9]. Electrothermal actuators have the advantages of large output force and low exciting voltage. But the response speed is slow because of the thermal

†These authors contributed equally to this work.
*Corresponding author (email: liuyingxiang868@hit.edu.cn)

expansion actuation principle, and their characteristics are greatly affected by environmental temperature and air flow [10]. Compared with these novel actuators, piezoelectric actuators are widely considered as precision actuators due to their advantages such as high precision, fast response, compact structure and no electromagnetic interference [11–14].

According to the working states, piezoelectric actuators can be classified into resonant type and non-resonant type. The resonant type operates near the resonant frequency of the piezoelectric vibrator and has characteristics such as fast movement and high output power [15–17]. However, high-frequency resonant vibration results in heat and wear, leading to poor accuracy and stability of the resonant type. The non-resonant type, on the other hand, operates at low frequency and can achieve relatively high accuracy. As a result, it is widely used in high-precision driving applications. According to the working principle, the non-resonant type piezoelectric actuators can be further divided into direct driven type, inchworm type, and inertial type. The direct driven type usually has simple excitation schemes and structure. The travel is tens of micrometers with high displacement resolution, since it directly uses a piezoelectric stack as the driving element [18,19]. In order to expand the travel range, travel amplification mechanisms are used, and the travel can reach hundreds of microns. However, the hundreds of microns travel range cannot meet the requirements of most applications. The inchworm type uses the "clamping-feeding" mechanism to achieve unlimited travel through continuous steps [20,21]. However, multiple actuators are generally required for driving, so that the structure and exciting signals are complex. The inertial type utilizes the periodic friction between the mover and the actuator to move. With the accumulation of single step motion, infinite travel can be achieved [22,23]. Compared with the other actuators, the inertial type is advantageous with the merits of compact structure, simple excitation scheme and large travel range.

However, due to the working principle of inertial type piezoelectric actuators, different friction states are required in the process of forward and backward. To realize the different friction states between forward and backward, inertial type piezoelectric actuators are generally designed as asymmetric structures [24–26] or apply asymmetric exciting signals [27,28]. If the asymmetric structure is adopted, the signals will be simple, while the inertial type piezoelectric actuators can only move in one direction. If asymmetric exciting signals are applied, a bulky power control system is required. For example, the piezoelectric controller (E53.D1S) produced by Harbin Core Tomorrow Science and Technology Co., Ltd. measures 148 mm×80 mm×27 mm in size. Similarly, the piezoelectric controller (E-873.10C885) manufactured by Physik Instrumente (PI Shanghai) Co., Ltd. is 186 mm×128 mm×20 mm in dimensions. These large sizes pose challenges for power integration and both devices require a 24 V power supply, necessitating the use of an additional power adapter. Besides, rollback motion is another problem of inertial type piezoelectric actuators due to the stick-slip operating mechanism. Several methods have been proposed to suppress the rollback motion of inertial type piezoelectric actuators. Adjusting the friction between the actuator and the mover is an effective method [29,30]. Generally, the friction force is adjusted by the preload, which requires a special preload adjustment mechanism and complicates the miniaturization and integration of the system. The principle of ultrasonic friction reduction can be applied by superimposing a composite waveform on the sawtooth wave exciting signal, which effectively reduces the rollback motion [31,32], but introduces unstable vibrations and increases signal complexity. Parasitic motion can also suppress the rollback motion. During the backward phase of the mover, the parasitic motion is used to generate positive friction to suppress the rollback motion [33]. This strategy is simple, but a larger mechanical structure is needed to generate parasitic motion.

To address the stick-slip driving rollback issue and the complex exciting signal waveform, a novel BRPA with symmetrical piezoelectric driving feet and a customized small power supply is proposed. By employing the proposed alternate excitation strategy, the friction force among the symmetrical driving feet and the output platform can be coordinated. This coordination ensures that the resultant friction force remains aligned with the direction of motion and effectively suppresses rollback movement. The customized small power supply, measuring a mere 58 mm×56 mm×46 mm, is capable of generating sawtooth wave signals to excite the rotation of the BRPA. In addition, both a single-step mode and a continuous mode are designed, enabling precise and rapid motion control. This work not only miniaturizes the actuator but also the power supply, providing a fresh perspective on miniaturizing piezoelectric actuators.

2 Design of BRPA and power supply

The design flowchart of the proposed BRPA and customized small power supply is shown in Figure 1. Firstly, the structure and working principle of the actuator are determined based on the requirements for high precision and compact structure. Then, the actuation principle of the actuator is analyzed. Next, a static model of the piezoelectric driving foot is established to investigate the relationship between the displacement of the piezoelectric driving foot, the amplitude of the exciting signal, and the structural parameters. Subsequently, the structural parameters are adjusted based on the observed influence, and the final structural parameters of the piezoelectric driving foot are determined through finite ele-

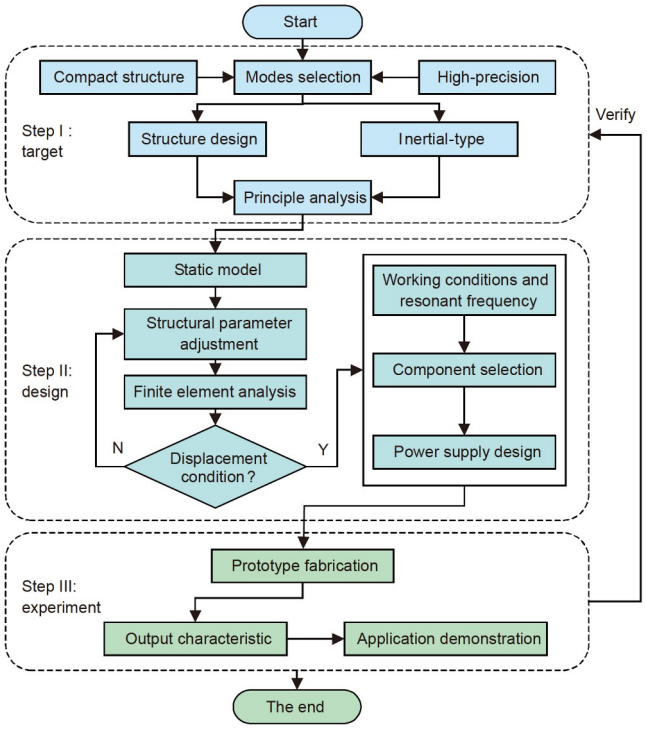

Figure 1 (Color online) The design flowchart of BRPA and power supply.

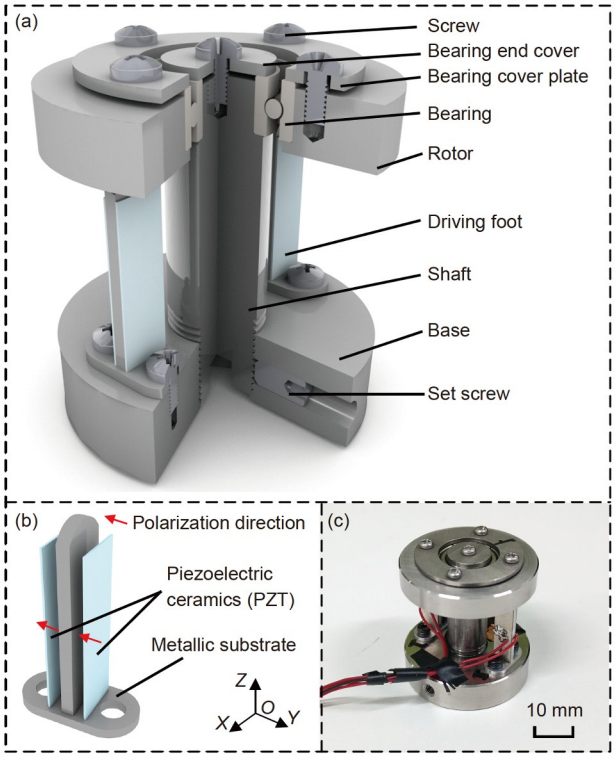

Figure 2 (Color online) The structure of BRPA and the configuration of driving foot. (a) The structure of BRPA; (b) the configuration of driving foot; (c) the prototype of BRPA.

ment simulation, including the resonant frequency. Following that, based on the operating conditions of the BRPA, the design specifications for a power supply are determined. Suitable electronic components are selected, and a customized small power supply is designed and fabricated. Finally, a prototype is fabricated and the output characteristics of the prototype are tested.

2.1 Structure of BRPA

The configuration of the BRPA is shown in Figure 2(a), including a rotor, a base, a shaft, a bearing, and two symmetrically configured driving feet. The bearing is used to connect the shaft and rotor, so that the rotor can rotate around the shaft. As the axial force on the bearing is very small, a precision deep groove ball bearing can be selected. The symmetrically configured driving feet are fixed on the base which is connected with the shaft through screw thread. The distances among the driving feet and the rotor can be adjusted by manipulating the screw thread to exert preload on the rotor. The radial set screw is used to fix the relative position between the base and the rotor when the preload force is determined.

The configuration of the driving foot and the polarization direction of piezoelectric ceramics are shown in Figure 2(b). The driving foot is formed by bonding two piezoelectric ceramics on a metallic substrate. When the exciting signal is applied, the piezoelectric ceramic on one side of the driving foot extends while the other side shortens, and the driving foot can bend towards the shortened side. By changing the polarity of the exciting signal, the bending direction of the piezoelectric driving foot can be reversed.

2.2 Principle analysis of BRPA

The force provided by a single driving foot is analyzed first. The forces on the rotor, as shown in Figure 3(a), primarily include the positive pressure N, the sum of the support force of the bearing and the gravity of the rotor N_g, the sum of the load moment and the bearing friction moment T_g, and the driving force of the driving foot F. The exciting signal of the single driving foot is shown in Figure 3(b). According to the force state of the rotor, the motion of the rotor is divided into three stages.

Original state At time t_a, the voltage of the signal applied to the driving foot is 0. The driving foot keeps still, so the driving force F is 0. At this time, the rotor is only affected by the force in the vertical direction.

Stick state From time t_a to t_b, the voltage rises from 0 to $U_{\max}$ slowly. The driving foot bends slowly to generate a driving force F perpendicular to the radial direction. At this time, if the rotor sticks to the driving foot and moves together, the expected inertia moment M_e is less than the maximum friction moment $M_{f,s,\max}$. The relationship of the

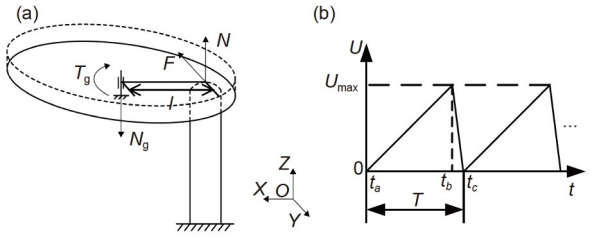

Figure 3 The operation principle of BRPA with a single driving foot. (a) The force of BRPA; (b) the signal applied to the driving foot.

rotor force along circumferential direction is as follows:

$$M_e = J\frac{\ddot{x}(t)}{l}, \tag{1}$$

$$F_{f,s,\max} = \mu_s N, \tag{2}$$

$$M_e < M_{f,s,\max} = F_{f,s,\max} \cdot l - T_g, \tag{3}$$

where J is the rotational inertia of the rotor, $\ddot{x}(t)$ is the linear acceleration at the end of driving foot, l is the distance from contact point to rotor center, $F_{f,s,\max}$ is the maximum static friction, μ_s is the static friction coefficient.

Slip state From time t_b to t_c, the voltage decreases from $U_{\max}$ to 0 rapidly, and the driving foot moves and returns to the initial position immediately. If the rotor sticks to the driving foot and moves together, the expected inertia moment M_e is larger than the moment provided by the driving force, so the rotor slips relative to the driving foot. The relationship of the rotor force along circumferential direction is as follows:

$$F_{f,d} = \mu_d N, \tag{4}$$

$$M_e > M_{f,d} = F_{f,d} \cdot l - T_g, \tag{5}$$

where $F_{f,d}$ is the dynamic friction, μ_d is the dynamic friction coefficient.

According to the analysis of the two states, the condition for relative slip between the driving foot and the rotor is

$$\ddot{x}(t) > \frac{\mu_s N \cdot l - T_g}{J} l. \tag{6}$$

During a motion cycle, BRPA with a single driving foot experiences a stick state and a slip state and produces a step angular displacement. The rotor can be continuously actuated by repeating more periods of the exciting signal.

As analyzed above, when there is only one driving foot, the rotor will roll back as the driving foot recovers. Since the maximum static friction force is greater than the dynamic friction force, when multiple driving feet coordinate their movements in a certain way, the total frictional force can always be kept forward, thereby suppressing rollback. The more driving feet there are, the more complex the structure of the actuator and the more exciting signals are required. Moreover, due to processing errors, it is difficult to ensure consistency among multiple driving feet. Two driving feet are the minimum number of driving feet to ensure this coordinated movement. Therefore, a structure with two driving feet is selected and it is beneficial for simplifying the structure and reducing power requirements.

In order to illustrate the schematic diagrams clearly, the spatial relationship among the driving feet and the rotor is changed from a three-dimensional space to a two-dimensional plane, as shown in Figure 4(a). Furthermore, the upper and lower driving feet are named legs I and II, respectively. The signals applied to the driving feet and the motion process of the actuator are shown in Figure 4(b) and (c), respectively. According to the different motion states of the two driving feet, the motion of the actuator within one cycle can be divided into four steps as follows.

Step 1 From t_a to t_b, the voltage of the signals applied to legs I and II increases slowly. The legs I and II bend counterclockwise slowly, so that there is sticking motion between legs I and II and rotor. Rotor rotates counterclockwise with the legs I and II.

Step 2 From t_b to t_c, the voltage of the signal applied to leg I decreases fast and that to leg II increases slowly. The leg I bends clockwise fast and the leg II bends counterclockwise slowly, so that there is slipping motion between leg I and rotor and sticking motion between leg II and rotor. Therefore, rotor rotates counterclockwise with the leg II.

Step 3 From t_c to t_d, similar to step 1, the voltage of the signals applied to legs I and II increases slowly, so rotor rotates counterclockwise with the legs I and II.

Step 4 From t_d to t_e, similar to step 2, the voltage of the signals applied to leg I increases slowly while that to leg II decreases fast, so rotor rotates counterclockwise with the leg I.

The rotor rotates without rollback when the exciting signals are applied continuously. The direction of rotation can be reversed by changing the asymmetry of the exciting signals. The process details can be seen in the Video S1 in Supporting Information.

2.3 Static model of driving foot

The displacement of the rotor is approximately equal to the static displacement at the end of the piezoelectric driving feet under static friction conditions. Therefore, the magnitude of the static displacement will affect the single step displacement of the BRPA. A static model for the piezoelectric driving foot is established to investigate the relationship between structural parameters, exciting signal amplitude, and the displacement of the piezoelectric driving foot. It can be used to determine the final structural parameters of the piezoelectric driving foot.

The structure of the piezoelectric driving foot is shown in Figure 5. The length of the piezoelectric driving foot can be divided into two sections, namely the bending section l_1 and the unbending section l_2, respectively. The output displace-

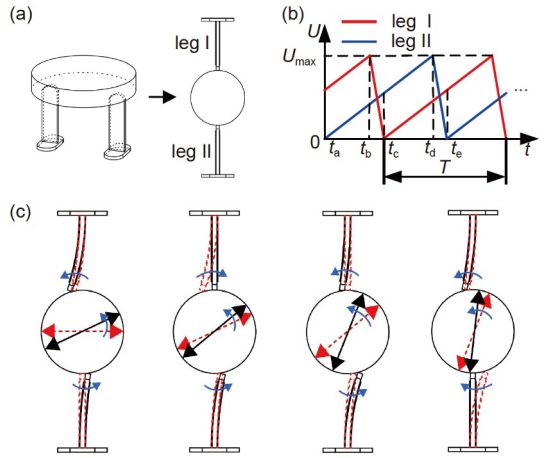

Figure 4 (Color online) The operation principle of BRPA. (a) Schematic diagram for transforming the three-dimensional spatial relationship into two-dimensional plane; (b) the signals applied to the driving feet; (c) the motion process of the BRPA in one cycle.

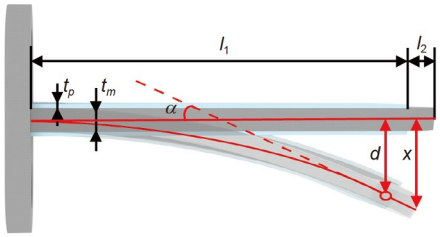

Figure 5 (Color online) Schematic of the piezoelectric driving foot bending.

ment of the piezoelectric driving foot x is the sum of the displacement of the bending section caused by the piezoelectric ceramics and the displacement amplified by the unbending section. Thus, the following relationship can be obtained:

$$x = \delta + l_2 \sin\alpha, \tag{7}$$

where δ is the displacement of the bending section, α is the angle of bending section.

Referring to the constitutive equations of symmetrical triple layer piezoelectric benders [34], the bending displacement equation of the piezoelectric driving foot can be derived:

$$\begin{bmatrix}\alpha\\ \delta\end{bmatrix} = \begin{bmatrix} \frac{12 s_{11}^m s_{11}^E l_1}{Dw} & \frac{6 s_{11}^m s_{11}^E l_1^2}{Dw} & \frac{6 s_{11}^m d_{31}(t_m+t_p) l_1}{D} \\ \frac{12 s_{11}^m s_{11}^E l_1^2}{Dw} & \frac{4 s_{11}^m s_{11}^E l_1^3}{Dw} & \frac{6 s_{11}^m d_{31}(t_m+t_p) l_1^2}{D} \end{bmatrix} \begin{bmatrix} M \\ F \\ V \end{bmatrix}, \tag{8}$$

$$D = 2 s_{11}^m (3 t_m^2 t_p + 6 t_m t_p^2 + 4 t_p^3) + s_{11}^E t_m^3, \tag{9}$$

where s_{11}^m and t_m are the compliance and thickness of the metallic substrate, respectively; s_{11}^E, d_{31}, and t_p are the compliance in a constant electric field, the transverse piezoelectric coefficient and thickness of the piezoelectric ceramics, respectively; w is the width of the metallic substrate and piezoelectric ceramics; M, F, and V are the external moment, the external tip force, and the applied electric voltage, respectively.

Due to the small bending angle of the driving foot, it can be considered that $\sin\alpha \approx \alpha$, the following relationship can be derived:

$$x \approx \begin{bmatrix} l_2 & 1 \end{bmatrix} \begin{bmatrix} \frac{12 s_{11}^m s_{11}^E l_1}{Dw} & \frac{6 s_{11}^m s_{11}^E l_1^2}{Dw} & \frac{6 s_{11}^m d_{31}(t_m+t_p) l_1}{D} \\ \frac{12 s_{11}^m s_{11}^E l_1^2}{Dw} & \frac{4 s_{11}^m s_{11}^E l_1^3}{Dw} & \frac{6 s_{11}^m d_{31}(t_m+t_p) l_1^2}{D} \end{bmatrix} \begin{bmatrix} M \\ F \\ V \end{bmatrix}. \tag{10}$$

When the driving foot is not affected by external moment and external tip force, the displacement of the driving foot can be obtained:

$$x = \frac{6 s_{11}^m d_{31}(t_m+t_p)(l_1 l_2 + l_1^2) V}{2 s_{11}^m (3 t_m^2 t_p + 6 t_m t_p^2 + 4 t_p^3) + s_{11}^E t_m^3}. \tag{11}$$

From eq. (11), the sensitive parameters of the displacement can be obtained. There is a linear relationship between the displacement and the voltage. Moreover, the output displacement increases with the length, and decreases with the thicknesses of the metallic substrate and the piezoelectric ceramics. The width hardly affects the displacement. As a result, these relationships can be used as the basis for determining the structural parameters.

2.4 Simulation of driving foot

The static model can provide a reference to determine the size of the piezoelectric driving foot, but there are simplifications and approximations in the process of establishing the static model. A finite element analysis model is established to verify the static model and optimize the structural dimensions. The material of the piezoelectric ceramics is selected as PZT-5. The metallic substrate is made of duralumin alloy (2A12). The parameters of the above materials are presented in Table 1 and the material constants of PZT-5 can be found in eqs. (12)–(14), where [**c**], [**e**], and [**ε**] are the stiffness matrix, the piezoelectric matrix, and the dielectric matrix, respectively.

The high working voltage of the actuator will pose a challenge to the design of the customized small power supply, and 50 V is selected as the working voltage of the actuator. The typical displacement range for the driving foot of a stick-slip actuator is 5 to 10 μm, as presented in previous work. Therefore, the output displacement of the driving foot is designed to 8 μm when a 50 V voltage exciting signal is applied. According to the simulation results, the dimensions of the piezoelectric driving foot are adjusted to meet the requirements of displacement and strength. The optimized dimensions are listed in Table 2. The simulation results are

Table 1 Material characteristics of driving foot

Parameter	Values
The Poisson's ratio of 2A12	0.33
The Young's modulus of 2A12	72 GPa
The density of 2A12	2810 kg/m^3
The density of PZT-5	7450 kg/m^3

Table 2 Main dimensions of driving foot

Symbol	Description	Values (mm)
l_1	Length of the piezoelectric ceramics	16
ω_p	Wide of the piezoelectric ceramics	5
t_p	Thickness of the piezoelectric ceramics	0.2
l_2	Length of the unbending segment	2
ω_m	Width of the metal substrate	5
t_m	Thickness of the metal substrate	1.2

shown in Figures 6 and 7, respectively.

$$[\mathbf{c}] = \begin{bmatrix} 12.72 & 8.02 & 8.47 & 0 & 0 & 0 \\ 8.02 & 12.47 & 8.47 & 0 & 0 & 0 \\ 8.47 & 8.47 & 11.74 & 0 & 0 & 0 \\ 0 & 0 & 0 & 2.34 & 0 & 0 \\ 0 & 0 & 0 & 0 & 2.3 & 0 \\ 0 & 0 & 0 & 0 & 0 & 2.3 \end{bmatrix} \times 10^{10}\ \mathrm{N/m^2}, \tag{12}$$

$$[\mathbf{e}] = \begin{bmatrix} 0 & 0 & -6.62 \\ 0 & 0 & -6.62 \\ 0 & 0 & 23.24 \\ 0 & 0 & 0 \\ 0 & 17.03 & 0 \\ 17.03 & 0 & 0 \end{bmatrix} \mathrm{C/m^2}, \tag{13}$$

$$[\boldsymbol{\varepsilon}] = \begin{bmatrix} 1704 & 0 & 0 \\ 0 & 1704 & 0 \\ 0 & 0 & 1433 \end{bmatrix} \times 10^{-11}\ \mathrm{F/m}. \tag{14}$$

When the static deflection of the piezoelectric driving foot is analyzed, the piezoelectric ceramics are bonded to the metallic substrate, and the bottom of the driving feet is fixed. By applying a voltage of 50 V to the piezoelectric ceramics, the static displacement and stress distribution of the piezoelectric driving feet are obtained, as shown in Figure 6. The maximum displacement is 8.27 μm. The maximum stress occurs at the connection of the cantilever beam and the base, which is 11.2 MPa, below the yield strength of 200 MPa.

The actuator operates at non-resonant frequency, so modal simulation is also carried out. As shown in Figure 7, the first three order resonance frequencies are 3390, 4516 and 20425 Hz, respectively. In order to ensure that the actuator operates in a stepping manner, the frequency of the exciting signals should be much lower than the first order resonance frequency.

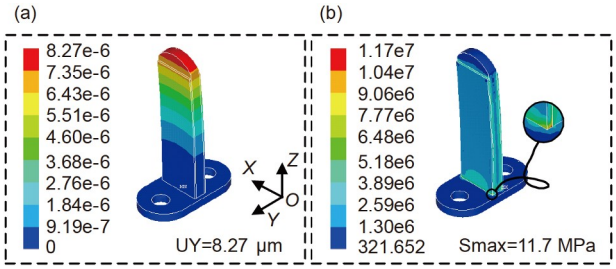

Figure 6 (Color online) Static mechanics simulation results of the piezoelectric driving foot (the voltage of 50 V is applied). (a) Displacement; (b) stress.

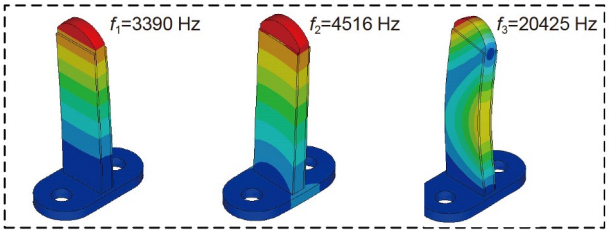

Figure 7 (Color online) Corresponding vibration mode of the first three orders resonance frequency.

2.5 Design of power supply

Sawtooth signal is required as BRPA goes through a stick stage and a slip stage in one cycle. At present, the power supply is mostly the combination of signal generators and power amplifiers, which results in large volume and high cost, restricting the application in miniaturized precision systems. In order to take advantage of the compact structure of BRPA, a customized small power supply is proposed and designed.

The system diagram of the customized small power supply is shown in Figure 8(a). The power supply is mainly composed of DC-DC converter, controller and amplifier, which is powered by a 5 V lithium battery. The XL6008 chip is used for the DC-DC converter, which can withstand a wide input voltage range of 3.6 to 32 V, and has a maximum output voltage of up to 60 V. The DC-DC converter converts the 5 V voltage of the lithium battery into ±45 V to power the amplifier. The controller adopts the STM32F103RCT6 chip, which has two independent DAC conversion channels and two DMA channels, and can control the two output channels. The controller is used to generate small amplitude sawtooth wave signals, and the amplitude, phase, and frequency of the signals can be controlled through the function keys on the power control panel. The OPA454 operational amplifier chip is selected for the amplifier, which can withstand a maximum voltage of 100 $V_{p\text{-}p}$. The amplifier amplifies the small amplitude signals output by the controller and applies it to the

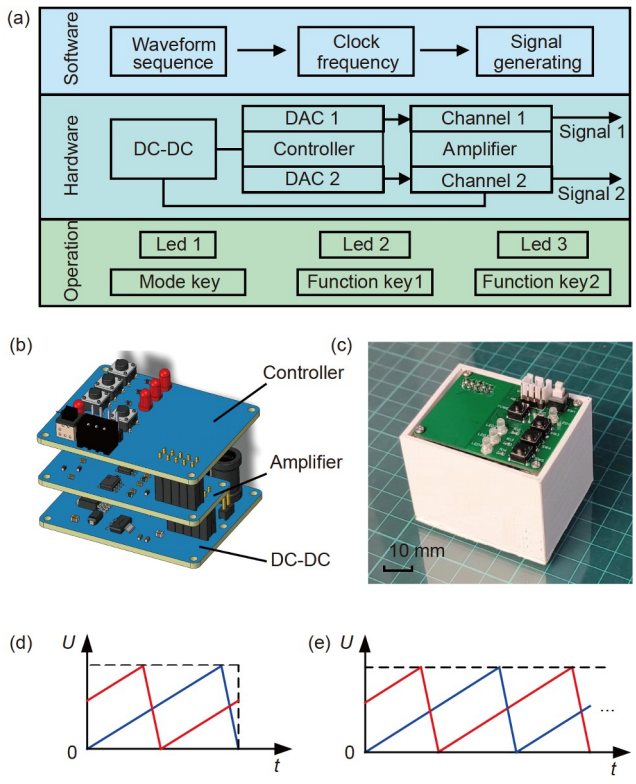

Figure 8 (Color online) The structure and operation modes of the customized small power supply. (a) The system block diagram; (b) the circuit board; (c) the prototype; (d) the single step mode; (e) the continuous mode.

BRPA. Finally, the prototype of the customized small power supply is manufactured, and the circuit board and prototype are shown in Figure 8(b) and (c), respectively. The size of the power supply is 58 mm×56 mm×46 mm.

The customized small power supply is equipped with two output channels that can adjust the signal phase to meet the needs of BRPA. The amplitude, frequency and asymmetry of the output signals can be adjusted by pressing the keys on the power supply to realize the speed regulation and reversal of BRPA. In addition, to achieve both rapid and precise motion, the power supply is designed with single step mode and continuous mode. The output signals for these two operating modes are shown in Figure 8(d) and (e), respectively. In single step mode, a single sawtooth wave signal is outputted when the power supply is triggered, and the BRPA responds by producing stepwise rotational motion to achieve fine positional adjustments. In continuous mode, a continuous sawtooth wave signal is outputted, and the BRPA rotates continuously until the power supply is triggered to stop.

3 Experiment and discussion

3.1 Experimental setup

A prototype of BAPA is manufactured according to the parameters in Table 2. As shown in Figure 2(c), the prototype is 35 mm in height and 32 mm in diameter. In order to investigate the output characteristics of the proposed BRPA, an experimental system is established and a series of experiments are carried out. Since the rotation angle is very small, it can be determined by

$$\theta \approx \frac{l}{r}, \tag{15}$$

where θ is the rotation angle of the prototype, l is the linear displacement of the rotor measured by the laser displacement sensor, r is the measuring radius.

The established experimental system is shown in Figure 9. The signals are generated by the function generator (DG4162, Beijing RIGOL Technology Co., Ltd, China), and amplified to the required amplitude by the power amplifier (E00. A3, Harbin Core Tomorrow Science and Technology Co., Ltd, China). The displacement is measured by a laser displacement sensor (LK-H020, Keyence, Japan), and the collected data is transmitted to the computer through the controller for processing. The laser displacement sensor has a resolution of 3 nm, a sampling frequency of 392 kHz. For the resolution measurement, a higher-precision capacitive displacement sensor (D-E20.050, PI, Germany) is used. The capacitance displacement sensor has a resolution of 1 nm and a sampling frequency of 1.24 kHz.

To quantify the phenomenon of rollback, we introduce the concept of "rollback ratio" to describe the degree of rollback. The formula for the rollback ratio is as follows:

$$R = \frac{S_{\text{rollback}}}{S} \times 100\%, \tag{16}$$

where R is the rollback ratio, S_{rollback} is the rollback of the rotor, S is the step angle of the rotor.

During the experiment, there are interference signals in the collected data due to noise and vibration, and the smooth filtering is used to reduce random interference and improve the readability of data.

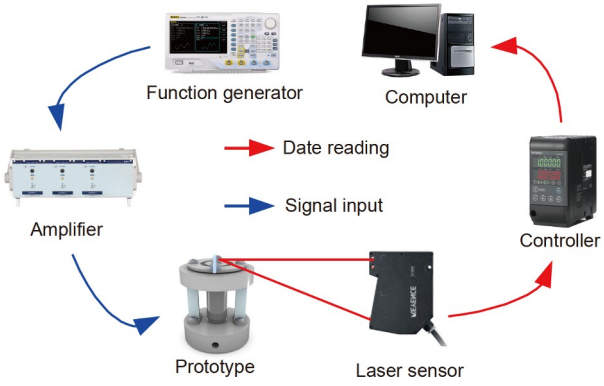

Figure 9 (Color online) The experimental setup used to test output characteristic of the proposed BRPA.

3.2 Experiment of piezoelectric driving feet

At first, the characteristics of the piezoelectric driving feet are measured. The output response characteristics of the piezoelectric driving feet are tested under a rectangular wave signal, the voltage amplitude and frequency are set as 50 V and 1 Hz, respectively. The experimental results are presented in Figure 10(a). The maximum output displacement is 8 μm at the voltage of 50 V, which is consistent with the simulation result. The driving foot responds quickly when the rectangular wave changes suddenly. The measure response time is shown in Figure 10(b), and it is less than 0.2 ms.

In order to prevent the driver feet from resonance to affect the output performance of BRPA, the first order resonant frequencies of the driving feet are tested. Sine scanning signal of 0–5 kHz is applied to the driving feet. The displacement data are collected, and the spectrograms are obtained through fast Fourier transform, which are plotted in Figure 10(c) and (d). The first resonant frequencies of the two driving feet are about 3.2 kHz, which show the consistency of the characteristics of the driving feet.

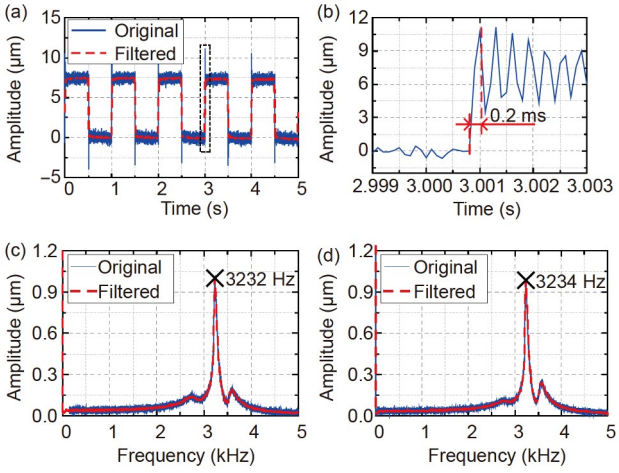

Figure 10 (Color online) Motion characteristics of piezoelectric driving feet. (a) The response characteristics of 50 V rectangular wave applied; (b) the amplified image of the response characteristics curve; (c), (d) the spectrograms of leg I and leg II.

3.3 Experiment of BRPA

Experiments of the BRPA prototype are tested to investigate the output characteristics, and the experimental results are presented in Figure 11. The relationship between the output performance and the voltage is tested by applying sawtooth signals with frequency of 1 Hz and phase difference of 0° to the prototype. When the voltage of the signals is below 10 V, the rotational motion of the prototype becomes unstable. Therefore, the voltage range of the exciting signals is chosen to be within 10–50 V. The rotation angle of the prototype is shown in Figure 11(a), and it can be seen that stable motions are generated. As shown in Figure 11(b), the net step angle of the prototype increases with the amplitude of the signal. When the voltage of the signal is 50 V, the prototype can produce the maximum net step angle of 0.717 mrad. With the increase of the voltage, the rollback ratio decreases first and then increases. When the voltage is 20 V, the rollback ratio is 0. This is because the step angle of the rotor is increased with the voltage. The larger step angle increases the initial velocity of the rotor in the slip state, while the deceleration time and acceleration are unchanged. Thus, the rollback angle is reduced with the increase of voltage, which causes the decrease of the rollback ratio. However, when the voltage increases from 20 to 50 V, the rollback ratio increases to 9.21%. This is because the impact vibrations of the driving feet are increased with the increase of the voltage, the deceleration time is significantly enlarged, which causes an increase in the rollback ratio.

The relationship between the output performance of the prototype and the frequency of the signal is shown in Figure 11(c) and (d). The signals' amplitude and phase difference remain at 50 V and 0°, respectively, while the frequency increases from 1 to 600 Hz. The rotation angle of the prototype is shown in Figure 11(c). It can be seen that when the frequency is low, the prototype outputs stable motion. When the frequency is too high, the output curve appears obvious bending and the motion is unstable. As shown in Figure 11(d), when the frequency is low, the net step angle of the prototype is almost unchanged. While when the frequency is too high, the net step angle decreases significantly. It indicates that when the frequency is high, the driving foot and the rotor cannot maintain synchronous motion in the stick state, but slip instead. When the frequency is low, the rotation velocity of the prototype increases as the frequency increases. However, when the frequency is high, the net step angle decreases, indicating that relative slipping occurs between the driving feet and the rotor in the stick state. As the frequency increases, the relative slipping intensifies, causing a decrease in the rotation velocity of BRPA. The experimentally measured maximum rotation velocity is 247 mrad/s, occurring at an exciting signal of 50 V and 550 Hz.

To verify the alternate excitation strategy of suppressing rollback, the exciting signals of the prototype have a certain phase difference. The frequency and amplitude of the signals remain 1 Hz and 50 V, respectively. The rotation angle of the prototype is shown in Figure 11(e), when the phase difference of signals is 0, the rotation angle has a very obvious rollback. With the phase difference increasing, the output curves become smooth. The influence of phase difference on the rollback ratio and net step angle is shown in Figure 11(f). It can be seen that with the increasing of the phase difference, the rollback ratio of the prototype decreases and the net step angle increases. When the phase difference is 180°, the

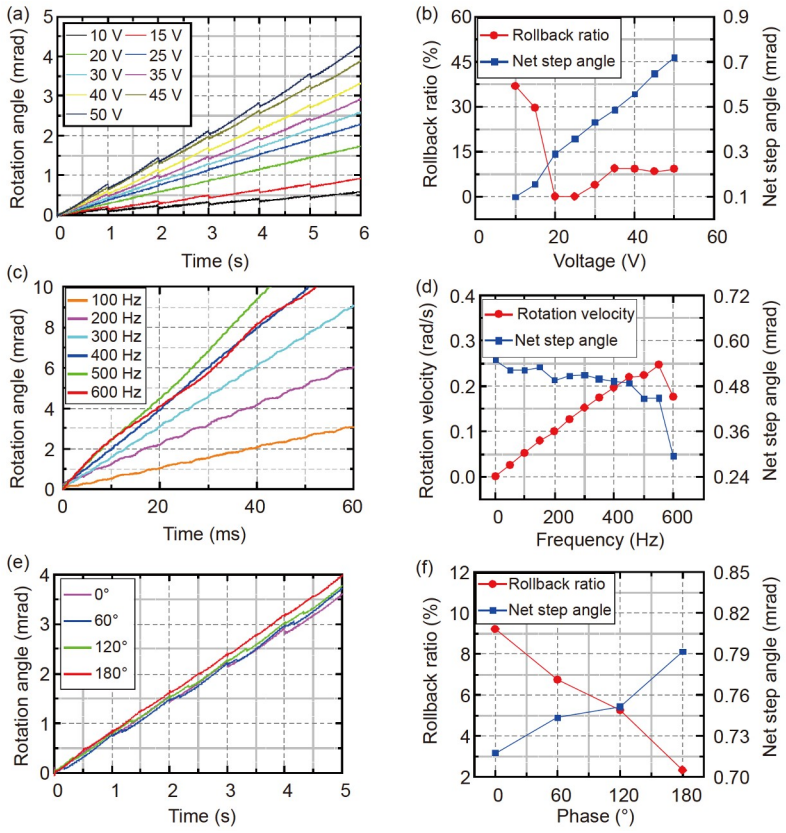

Figure 11 (Color online) Motion characteristics of BRPA. (a) Rotation angle versus time under different voltages; (b) the influence of voltage on rollback ratio and net step angle; (c) rotation angle versus time under different frequencies; (d) the influence of frequency on rotary velocity and net step angle; (e) rotation angle versus time under different phases; (f) the influence of phase on rollback ratio and net step angle.

rollback ratio is 2.34%. In the discussion of Figure 11(b), the rollback ratio is closely related to the voltage and frequency, so the displacement smoothness of the prototype will be affected when the speed is adjusted by frequency. However, when the signals with phase difference of 180° applied to the prototype, the rollback can be well suppressed under any circumstances.

Angular resolution is directly related to the precision of BRPA, which is tested by applying stepping signal increasing from 0 to 600 mV with an increment of 120 mV. The rotation angle of the prototype is shown in Figure 12. It can be seen that the angular resolution of the prototype is 0.66 μrad.

Then the characteristics with different torque and load are tested, respectively. The frequency and amplitude of the signals remain 2 Hz and 50 V, respectively. The torque characteristic is tested, and the torque is applied by hanging weights on the fixed pulley mechanism. The results are shown in Figure 13(a). The rotation velocity of the prototype decreases rapidly when the load torque is larger than 0.3 N mm. This is because the torque generated by the static frictions among the driving feet and the rotor is not enough to ensure them move synchronously. The slip in stick state so that the rotation velocity decreases. When the torque increases to 1.3 N mm, the rotary velocity is almost 0, that is, the stall torque of the prototype is 1.3 N mm. The load characteristic is tested by applying a weight on the top of the

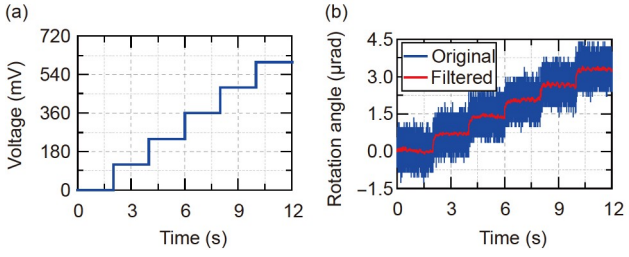

Figure 12 (Color online) Angular resolution of BRPA and the signal. (a) The signal applied to driving feet; (b) the response rotary angle.

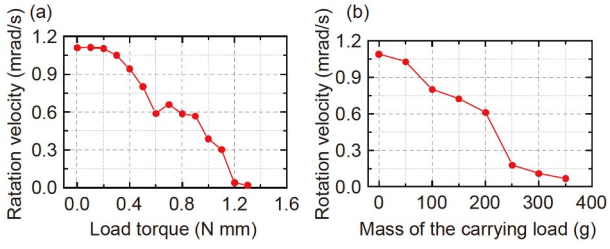

Figure 13 (Color online) Carrying load characteristic of BRPA. (a) The characteristic with different torques; (b) the characteristic with different loads.

prototype, as shown in Figure 13(b). The rotary velocity is almost 0 when the weight is 350 g, and the bearing capacity of the prototype is 350 g.

3.4 Demonstration of optical fiber alignment

To demonstrate the precise movement capability of the proposed BRPA and the performance of the customized small power supply, an application experiment of optical fiber alignment is conducted. The experimental setup is depicted in Figure 14(a), and the diameter of the optical fiber is 250 μm, which is divided into two parts. One part is fixed on the prototype and illuminated by a laser pointer, named as fiber 1, while the other is fixed on the bracket, named as fiber 2. As shown in Figure 14(c) and (d), when the fiber 1 is aligned with the head of the fiber 2, the tail of the fiber 2 will be lighted. In the experiment, the customized small power supply is used for open-loop control of the prototype, and the alignment situation is observed through a digital microscope. At the beginning, when the optical fibers are far away, the prototype rotates quickly to approach the optical fiber, as shown in Figure 14(b). When the distance is shortened, the speed of the prototype decreases. As shown in Figure 14(c), when the optical fiber appears in the field of vision of the digital microscope, the operation mode of the customized small power supply is adjusted from continuous mode to single step mode. The prototype runs in single step mode until the optical fiber is aligned, as shown in Figure 14(d). The experiment successfully verifies that the proposed BRPA and the customized small power supply can be used to adjust the rotational DOF of optical fiber in the scene of optical fiber alignment, and proves the application potential of the system in the precision fields.

Table 3 presents a comparison between the BRPA and other inertia type piezoelectric actuators. It can be observed that the BRPA exhibits a compact structure and requires a voltage of only 50 V, which helps to reduce the power supply requirements. Moreover, the BRPA demonstrates a lower rollback ratio of 2.34%, resulting in smoother displacement output. Due to the relatively low excitation voltage, a customized small power supply for the BRPA can be designed and powered by an independent lithium battery. In summary, the proposed BRPA offers a compact structure, low rollback, and convenient power supply.

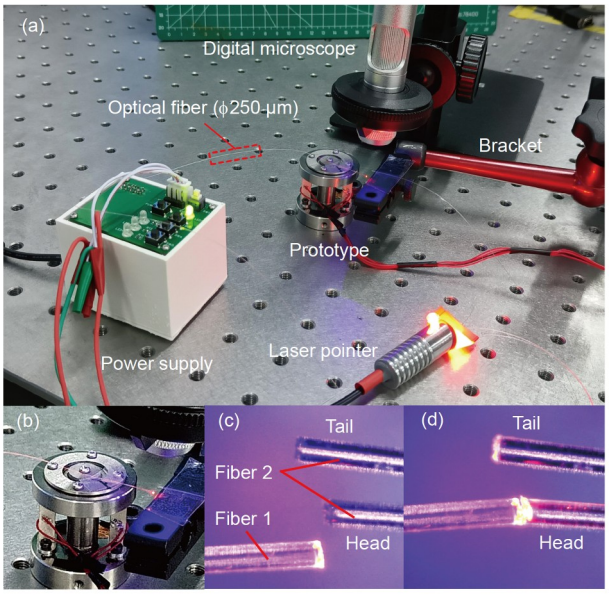

Figure 14 (Color online) BRPA is used in optical fiber alignment. (a) The experimental setup; (b) the optical fiber is divided into two parts, which are fixed on the prototype and the bracket, respectively, where the optical fiber fixed on the prototype is named as fiber 1, and the other is named as fiber 2; (c) when the fiber 1 and the head of fiber 2 are not aligned, there is no light at the tail of fiber 2; (d) when the fiber 1 and the head of fiber 2 are aligned, the tail of fiber 2 is lighted.

4 Conclusion

In this study, a bimorph rotary piezoelectric actuator with a customized small power supply is proposed. The structure is designed, the working principle is introduced, and the alternate excitation strategy for suppressing rollback is evaluated. The customized small power supply is designed and manufactured to excite the actuator. It can output signals for the single step mode and the continuous mode, and they are adopted to excite the actuator to achieve a small stroke with one single step and a large stroke with continuous step,

Table 3 Performance comparison with other inertial type piezoelectric actuators

Parameters	Deng et al. [1]	Cheng et al. [26]	Tian et al. [30]	This work
Size	Medium (230×Φ32 mm^3)	Large	Medium (118 mm×75 mm×41.5 mm)	Small (35×Φ32 mm^3)
Voltage	120 V	100 V	150 V	50 V
Bidirectional	Yes	No	Yes	Yes
Maximum speed	200.9 mrad/s	5.39 rad/s	4.18 mm/s	247 mrad/s
Maximum load	32 mN	3.62 N mm	9.3 kg	1.3 N mm
Resolution	30 μrad	14.3 μrad	4.16 nm	0.66 μrad
Rollback	Yes	Yes	0.94%	2.34%
Power supply	Universal	Universal	Universal	Customized (58 mm×56 mm×46 mm)

respectively. The characteristics of the actuator are measured, the maximum rotation velocity and the resolution are 0.247 rad/s and 0.66 μrad, the vertical bearing capacity and stall torque are 350 g and 1.3 N mm, which can meet the requirements of many precision fields. It is found that the phase difference of the exciting signals of the two driving feet has a great influence on the rollback ratio, which is almost zero when the phase difference of the exciting signal is 180°. The customized small power supply and the prototype are used to build a simple demonstration experiment system for optical fiber alignment. The experimental results indicate the practicability of the customized small power supply and the application potential of this work in the precision fields. In our future work, we will primarily focus on further structural optimization of the BRPA, as well as its motion control and exploration of specific applications.

This work was supported by the National Natural Science Foundation of China (Grant Nos. 52105015 and 52225501), the China Postdoctoral Science Foundation (Grant No. 2021M690830), and the Postdoctoral Science Foundation of Heilongjiang Province, China (Grant No. LBH-Z21018).

Supporting Information

The supporting information is available online at tech.scichina.com and link.springer.com. The supporting materials are published as submitted, without typesetting or editing. The responsibility for scientific accuracy and content remains entirely with the authors.

1 Deng J, Liu S, Liu Y, et al. A 2-DOF needle insertion device using inertial piezoelectric actuator. IEEE Trans Ind Electron, 2022, 69: 3918–3927
2 Zhang S, Liu Y, Deng J, et al. Development of a low capacitance two-axis piezoelectric tilting mirror used for optical assisted micromanipulation. Mech Syst Signal Process, 2021, 154: 107602
3 Feng Y, Liu J, Li K, et al. Waveform optimization of piezoelectric micro-jet for the control of metal micro-droplet ejection. IEEE Trans Ind Electron, 2022, 69: 3967–3976
4 Yang G, Yang L, Du J, et al. PN junctions with coupling to bending deformation in composite piezoelectric semiconductor fibers. Int J Mech Sci, 2020, 173: 105421
5 Zhang J Z, Tan X M. Experimental study on flow and heat transfer characteristics of synthetic jet driven by piezoelectric actuator. Sci China Ser E, 2007, 50: 221–229
6 Leveziel M, Haouas W, Laurent G J, et al. MiGriBot: A miniature parallel robot with integrated gripping for high-throughput micromanipulation. Sci Robot, 2022, 7: eabn4292
7 Kim W, Shin D, Chung C C. Microstepping using a disturbance observer and a variable structure controller for permanent-magnet stepper motors. IEEE Trans Ind Electron, 2013, 60: 2689–2699
8 Rasekh M, Khadem S E. Pull-in analysis of an electrostatically actuated nano-cantilever beam with nonlinearity in curvature and inertia. Int J Mech Sci, 2011, 53: 108–115
9 Morkvenaite-Vilkonciene I, Bucinskas V, Subaciute-Zemaitiene J, et al. Development of electrostatic microactuators: 5-year progress in modeling, design, and applications. Micromachines, 2022, 13: 1256
10 Potekhina A, Wang C. Review of electrothermal actuators and applications. Actuators, 2019, 8: 69
11 Mohith S, Upadhya A R, Navin K P, et al. Recent trends in piezoelectric actuators for precision motion and their applications: A review. Smart Mater Struct, 2020, 30: 013002
12 Wang L, Chen W, Liu J, et al. A review of recent studies on non-resonant piezoelectric actuators. Mech Syst Signal Process, 2019, 133: 106254
13 Zhang S J, Liu Y X, Deng J, et al. A novel sensitive piezoelectric mass balance used for weightless environment. Sci China Tech Sci, 2021, 64: 745–754
14 Chen Y H, Liu Y D, Liu T S, et al. Design and analysis of an untethered micro flapping robot which can glide on the water. Sci China Tech Sci, 2022, 65: 1749–1759
15 Deng J, Yang C L, Liu Y X, et al. Design and experiments of a small resonant inchworm piezoelectric robot. Sci China Tech Sci, 2023, 66: 821–829
16 Zhou T Y, Chen Y, Lu C Y, et al. Integrated lens auto-focus system driven by a nut-type ultrosonic motor (USM). Sci China Ser E-Tech Sci, 2009, 52: 2591–2596
17 Liu Y, Yan J, Wang L, et al. A two-DOF ultrasonic motor using a longitudinal-bending hybrid sandwich transducer. IEEE Trans Ind Electron, 2019, 66: 3041–3050
18 Xu Q. Design and development of a flexure-based dual-stage nanopositioning system with minimum interference behavior. IEEE Trans Automat Sci Eng, 2012, 9: 554–563
19 Zhang S, Zhao H, Ma X, et al. A 3-DOF piezoelectric micromanipulator based on symmetric and antisymmetric bending of a cross-shaped beam. IEEE Trans Ind Electron, 2023, 70: 8264–8275
20 Kim S C, Kim S H. Precise rotary motor by inchworm motion using dual wrap belts. Rev Sci Instrum, 1999, 70: 2546–2550
21 Yu H P, Liu Y X, Deng J, et al. A 3-DOF piezoelectric robot with continuous walking gait aiming at cross-scale smooth motion. Sci China Tech Sci, 2023, 66: 233–242
22 Deng J, Wang W, Zhang S, et al. An inertial bipedal piezoelectric actuator with integration of triple actuation modes. Smart Mater Struct, 2022, 31: 115019
23 Zhang S, Liu Y, Deng J, et al. Piezo robotic hand for motion manipulation from micro to macro. Nat Commun, 2023, 14: 500
24 Wen J, Ma J, Zeng P, et al. A new inertial piezoelectric rotary actuator based on changing the normal pressure. Microsyst Technol, 2013, 19: 277–283
25 Cheng G, Hu Y, Wen J, et al. Piezoelectric inertial rotary actuators based on asymmetrically clamping structures. Sens Actuat A-Phys, 2015, 223: 125–133
26 Chen K, Wen J, Cheng G, et al. An asymmetrical inertial piezoelectric rotary actuator with the bias unit. Sens Actuat A-Phys, 2016, 251: 179–187
27 Deng J, Liu Y, Li K, et al. Design, modeling, and experimental evaluation of a compact piezoelectric *XY* platform for large travel range. IEEE Trans Ultrason Ferroelect Freq Contr, 2020, 67: 863–872
28 Zhang S, Liu Y, Deng J, et al. Development of a two-DOF inertial rotary motor using a piezoelectric actuator constructed on four bimorphs. Mech Syst Signal Process, 2021, 149: 107213
29 Wang X, Huang H, Fan H, et al. Evolution of one-stepping characteristics of a stick-slip piezoelectric actuator under various initial gaps. Sens Actuat A-Phys, 2019, 295: 348–356
30 Tian X, Chen W, Zhang B, et al. Restraining the backward motion of a piezoelectric stick-slip actuator with a passive damping foot. IEEE Trans Ind Electron, 2022, 69: 10396–10406
31 Deng J, Liu Y, Li J, et al. Influence of multidirectional oscillations on output characteristics of inertial piezoelectric platform. IEEE ASME Trans Mechatron, 2022, 27: 4122–4131
32 Cheng T, Li H, He M, et al. Investigation on driving characteristics of a piezoelectric stick-slip actuator based on resonant/off-resonant hybrid excitation. Smart Mater Struct, 2017, 26: 035042
33 Yang Z, Zhou X, Huang H, et al. On the suppression of the backward motion of a piezo-driven precision positioning platform designed by the parasitic motion principle. IEEE Trans Ind Electron, 2020, 67: 3870–3878
34 Wang Q M, Cross L E. Constitutive equations of symmetrical triple layer piezoelectric benders. IEEE Trans Ultrason Ferroelect Freq Contr, 1999, 46: 1343–1351